

Rf strain-controlled built-in electric field near SiO₂/SiGe interface

Artem Podolian, Vasyl Kuryliuk, Oleg Korotchenkov *

Faculty of Physics, Taras Shevchenko Kyiv National University, 01601 Kyiv, Ukraine

ARTICLE INFO

Article history:

Received 18 February 2009

Received in revised form

23 June 2009

Accepted 10 July 2009

Available online 4 August 2009

Keywords:

Photovoltage

SiGe

Strain

ABSTRACT

We have found that rf strains remarkably affect the photovoltage in the Au/SiO₂/SiGe Schottky barrier. We have monitored spectra of photovoltage and DLTS spectra as a function of the amplitude of the strain applied to the SiGe/Si heterostructure. We have observed an inversion of the photovoltage produced by the strain accompanied by the quenching effect on DLTS peaks. We have argued that rf strains are capable of modifying a built-in electric field near SiO₂/SiGe interface which can be used for improvement of the power conversion efficiency in SiGe-based solar cells.

© 2009 Elsevier B.V. All rights reserved.

1. Introduction

Bulk crystalline SiGe alloys and Ge quantum dots grown on Si have attracted much interest as promising materials for the application in Si-based electronics and optoelectronics. One of the most noticeable applications is in solar cells with the objective of improving the cell sensitivity for photon energies below the bandgap of Si [1–3]. It has been found that, employing SiGe, there is a clear improvement in the long wavelength response relative to Si solar cells, but the decrease of open-circuit voltage and fill factor result eventually in a lower efficiency relative to the crystalline Si devices [4]. To improve the power conversion efficiency, a suitable built-in electric field E_{bi} with a desired direction in the device is necessary for better separation and collection of free carriers. An improper direction of E_{bi} could in turn accelerate recombination of free carriers, resulting in a lower power conversion efficiency.

In this work, an original method of altering the built-in electric field utilising rf strains is proposed. It is applied to oxidized SiGe layers grown on Si substrates, illustrating that high enough strains with a controllable spatial location of the strained patterns can be induced and making the strains potentially useful as an important design principle of integrated devices based on SiGe technologies.

Previously, a lot of effort has been put into the exploitation of ultrasonic treatment techniques in order to engineer and to recover defect-related electronic parameters of silicon [5]. In particular, dissolved defect clusters and defect pairs [6,7] enhanced diffusion [8], recovery of electrical conductivity [9]

and defect transformation [10] in irradiated Si have been achieved utilising ultrasonic treatments. Extensive studies on device performance affected by ultrasound, including leakage currents, current noise, solar cell efficiency and noise characteristics [5], as well as current–voltage curves [11], have also been performed.

2. Strain analysis of the composite structure piezoelectric–photoelectric material

An accurate modelling of rf strain fields arisen in the semiconducting structure (1 in Fig. 1) due to forced vibrations of the piezoceramic transducer (2) mounted on the sample surface requires the application of numerical methods. An rf voltage V supplied from a generator drives the transducer resulting in vibrations of the coupled materials 1 and 2. The rf strain is then produced in the semiconductor allowing to mechanically modify the electronic properties of the material.

Therefore, we first give a brief discussion of the strain computations done within the framework of the general finite element method (FEM) approach [12]. Here, since the thickness of the layers is much less than their length and width, the strain fields are analysed by two-dimensional (2D) simulations.

The governing equations coupling the electrical and mechanical quantities are

$$\begin{cases} T_{ij} = c_{ijkl}S_{kl} - e_{ijk}^T E_k, \\ D_i = e_{ijk}S_{jk} + \epsilon_{ij}E_j \end{cases} \quad (1)$$

for the piezoelectric layer 2 and

$$\begin{cases} T_{ij} = c_{ijkl}S_{kl}, \\ D_i = e_{ijk}S_{jk} \end{cases} \quad (2)$$

* Corresponding author.

E-mail address: olegk@univ.kiev.ua (O. Korotchenkov).

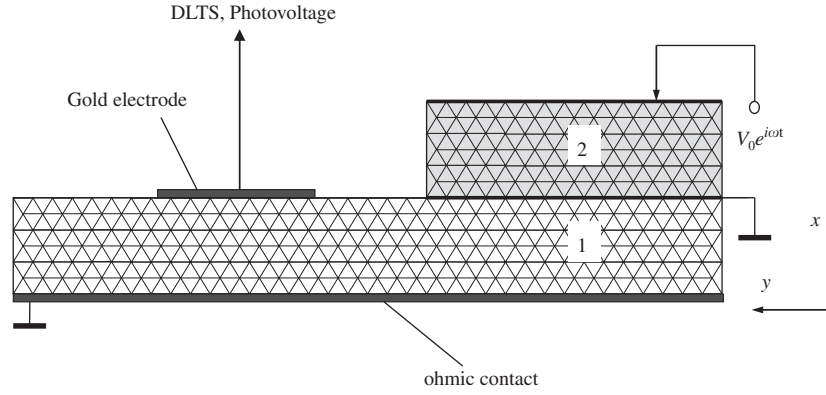


Fig. 1. The two-layer sandwich structure consisting of the photoelectric semiconductor (1) and the piezoceramic (PZT) (2) layers. A harmonic time dependence is assumed provided the vibrations are excited by an rf signal $V_0 e^{i\omega t}$, V_0 being the voltage amplitude and t the time.

for the semiconductor layer 1. Here T_{ij} and S_{kl} are the stress and the strain tensor components, c_{ijkl} , e_{ijk} and ε_{ij} are the elastic stiffness tensor, piezoelectric coefficient tensor and permittivity tensor components, the superscript T means transposing the row matrix, D_i and E_k are the electric displacement and the electric field vector components, respectively. The material parameters used here are given in Tables 1 and 2.

The mechanical boundary conditions imply the rigid inter-media interface, so that the T_{ij} and mechanical displacement U_i components are continuous at the interface whereas $T_{ij} = 0$ at free surfaces. A harmonic time dependence is assumed provided the vibrations are excited by an rf signal $V_0 \exp(i\omega t)$, V_0 being the voltage amplitude, t the time and ω the angular frequency. The rf signal is applied to metal electrodes covering the piezoceramic plate. The metal electrode layers are considered to be thin and do not influence the above boundary conditions for the stress tensor. Since the metal layer turned to the interface is grounded the coupling of the two materials 1 and 2 is purely mechanical. Therefore, the piezoelectric field $\vec{E} = -\vec{\nabla}\varphi$ (φ being the electric potential) is presumed to be zero inside the semiconductor.

Following the FEM discretization procedure, the structure in Fig. 1 is divided into small elements and the unknown functions U_i , φ inside the element are written as

$$\begin{pmatrix} U_x \\ U_y \\ U_z \\ \varphi \end{pmatrix} = \begin{pmatrix} N_1 & 0 & 0 & 0 & \dots & N_n & 0 & 0 & 0 \\ 0 & N_1 & 0 & 0 & \dots & 0 & N_n & 0 & 0 \\ 0 & 0 & N_1 & 0 & \dots & 0 & 0 & N_n & 0 \\ 0 & 0 & 0 & N_1 & \dots & 0 & 0 & 0 & N_n \end{pmatrix} \times \begin{pmatrix} \tilde{u}_{x1} \\ \tilde{u}_{y1} \\ \tilde{u}_{z1} \\ \tilde{\varphi}_1 \\ \vdots \\ \tilde{u}_{xn} \\ \tilde{u}_{yn} \\ \tilde{u}_{zn} \\ \tilde{\varphi}_n \end{pmatrix}, \quad (3)$$

where n is the number of the node points for each the element, N_i are the shape functions in the i -th node point. Based on the resulting finite element mesh, the FEM matrix equation is written as

$$\begin{pmatrix} K_{uu} & K_{u\varphi} \\ K_{\varphi u} & K_{\varphi\varphi} \end{pmatrix} \begin{pmatrix} \tilde{u} \\ \tilde{\varphi} \end{pmatrix} - \omega^2 \begin{pmatrix} M_{uu} & 0 \\ 0 & 0 \end{pmatrix} \begin{pmatrix} \tilde{u} \\ \tilde{\varphi} \end{pmatrix} = \begin{pmatrix} F \\ Q \end{pmatrix}, \quad (4)$$

Table 1

Material parameters of PZT (hexagonal, 6mm) used to calculate the stress fields, taken from Ref. [13].

Stiffness (10^{10} N/m ²)					Piezoelectric coefficients (C/m ²)			Relative permittivity	
C_{11}	C_{33}	C_{44}	C_{12}	C_{13}	e_{15}	e_{31}	e_{33}	ε_{11}	ε_{33}
13.5	11.3	2.22	6.79	6.81	17.0	−6.5	23.3	504	260

Table 2

Material parameters of Si (cubic, $m3m$) used to calculate the stress fields, taken from Ref. [13].

Stiffness (10^{10} N/m ²)			Relative permittivity
C_{11}	C_{44}	C_{12}	ε_{11}
16.57	7.956	6.39	11.7

where K and M are the stiffness and the mass matrices, respectively, and F and Q are the vectors of the mechanical and electrical node loads, respectively. Solving Eq. (4) allows us to find the strain and displacement fields throughout the structure of Fig. 1.

The structure vibrational spectra may be analysed in terms of the electrical admittance versus frequency dependence. A portion of this in the frequency range of our interest is shown in Fig. 2.

Fig. 3 shows the $S_{11} + S_{22}$ strain amplitude taken in the middle cross-section of the structure and calculated by the method of this work for the selected resonance frequencies displayed in Fig. 2. It is seen that the strained and dilated patterns seemingly resemble each ones in both cases, although their number taken along the semiconductor length increases with increasing the frequency. The value of the strain amplitude also varies with frequency, so that it is roughly 3 times greater in Fig. 3(b) compared to the one seen in Fig. 3(a). This observation together with the fact that the strain gradient obviously increases with frequency opens new opportunities to control the spatial location of the strained patterns, allowing to generate a driving force for modification of the electronic parameters in the semiconductor.

3. Experimental details

The data presented here were obtained with a 1- μ m thick $\text{Si}_{0.83}\text{Ge}_{0.17}$ layer grown by chemical vapour deposition with no

intentional doping on a 300- μm thick (100)Si substrate. There was no graded layer introduced on the SiGe/Si interface in order to compensate the lattice mismatch between SiGe and Si. For deep-level transient spectroscopy (DLTS) measurements, the Schottky barrier contact, 1 mm in diameter, was formed by thermal evaporation of gold on top of the oxide layer covering SiGe while the ohmic contact was formed on the back side of the sample, as shown in Fig. 1. Capacitance–voltage (C – U) measurements showed a shallow trap concentration of about $4 \times 10^{14} \text{ cm}^{-3}$.

The DLTS measurements were made using a DLS-83D spectrometer. The measurements were performed at reverse biases from 0 to 8 V in the temperature range between 77 and 300 K. The photovoltage signal in the SiGe/Si heterostructure was taken by illuminating the front surface with a tungsten lamp light

dispersed by a double prism monochromator. The sample temperature was measured with a Cu–Constantan thermocouple directly attached to the sample. Special care was taken to ensure that the experimental systems were not susceptible to electronic pickups or ground loop effects induced by rf signals introduced by acoustic techniques.

The rf voltage amplitude was continuously adjustable between $V_0 = 0$ and 35 V and the higher resonance frequency (cf. Fig. 2) was employed in the measurements given below.

4. Results and discussion

The DLTS spectrum shown in Fig. 4 (spectrum 1) has two dominant peaks labelled A and B with an activation energy of approximately 0.4 and 0.2 eV, respectively, obtained from the Arrhenius plots (Fig. 5). It has been verified that the strength of the peak B is sensitive to the presence of the oxide layer, implying the peak originate from the SiGe/SiO₂ interface region. Following the assignment made in previous studies [14] this peak can be ascribed to the Si–O– dangling bonds.

Among the reported defect levels in Si and SiGe, the dislocation and the divacancy are located at about 0.4 eV below the conduction band [15]. Since high densities of misfit dislocations are present in our samples to relieve the Si and Ge lattice mismatch strain, it is reasonable to relate peak A in Fig. 4 (spectrum 1) to dislocations.

Fig. 6 displays the evolution of the photovoltage spectrum with increasing V_0 whereas appropriate change in the band diagram of the Au/SiGe/Si structure is shown in Fig. 7. When the light energy $h\nu$ (h is Planck's constant and ν is incident light frequency) exceeds the energy gap E_{gSiGe} of the SiGe layer (≈ 1.08 eV at room temperature), electron–hole (e – h) pairs are generated in the Schottky barrier (process 1 in Fig. 7), separated by the local fields in the depletion layer (processes 2) and give rise to a photovoltage between the Au electrode and the bulk of a SiGe layer. When $h\nu$

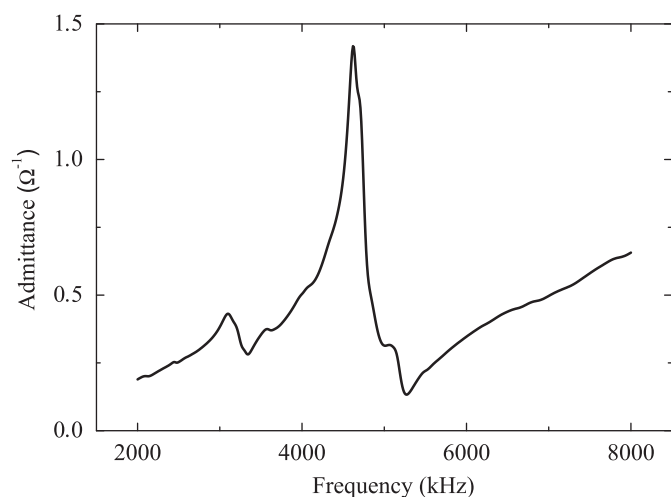


Fig. 2. Computed admittance versus frequency for the structure shown in Fig. 1 exhibiting two characteristic vibrational modes at 3104 and 4628 kHz.

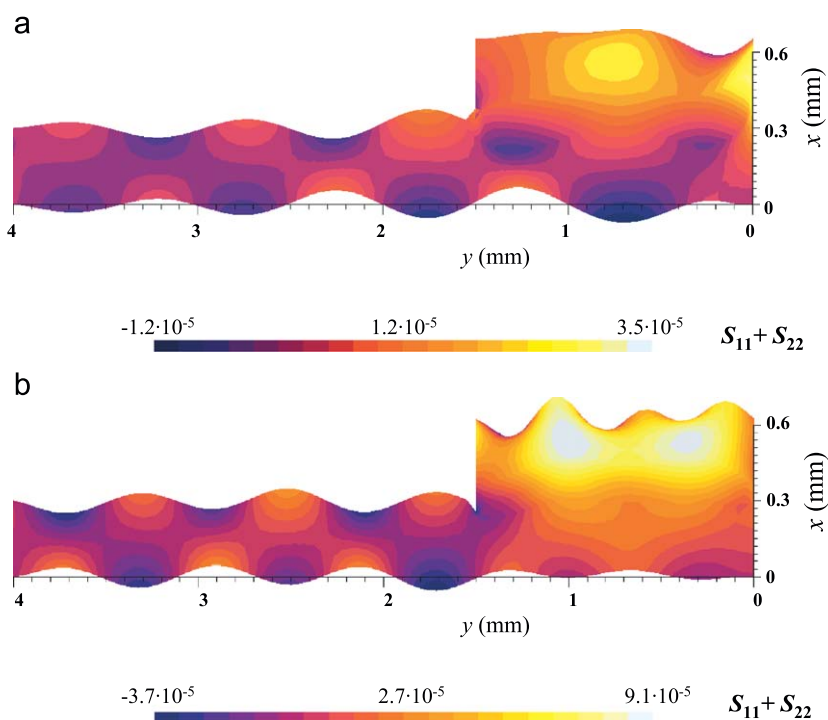


Fig. 3. Computed strain field ($S_{11} + S_{22}$) in the middle cross-section of the structure shown in Fig. 1 at the selected resonances of 3104 (a) and 4628 (b) kHz. The value $V_0 = 35$ V is taken in the computations.

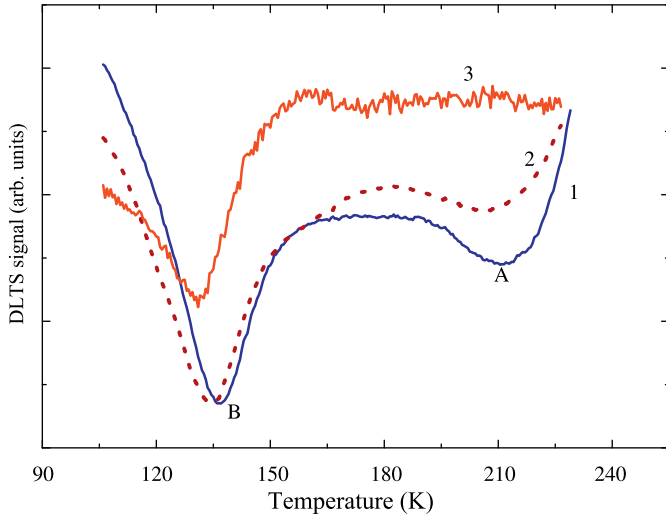


Fig. 4. DLTS spectrum of Au/SiGe/Si at $V_0 = 0$ (spectrum 1), 6 V (2), 23 V (3). Spectrum 3 is enlarged by a factor of 5 compared to spectra 1 and 2. Emission rate $e = 2513 \text{ s}^{-1}$, reverse bias voltage is 2 V.

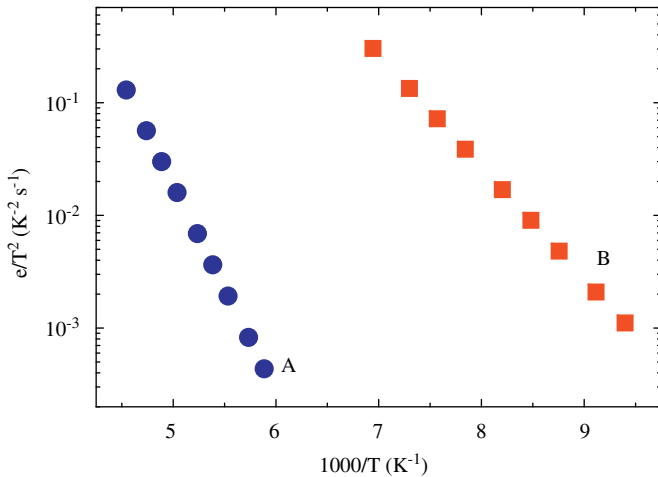


Fig. 5. T^2 -corrected thermal emission rates of the traps featuring in Fig. 4. Activation energies derived from the slope of the least mean square fit are 197 meV (peak B) and 366 meV (peak A).

becomes greater than E_{gSi} of the Si substrate ($\approx 1.15 \text{ eV}$), the generated $e-h$ pairs (process 3 in Fig. 7) are separated in the heterojunction region (processes 4) to develop an extra voltage which results in the enhanced signal above E_{gSi} in spectrum 1 of Fig. 6. Rf strain markedly affects the photovoltage signal; see spectra 2 and 3 in Fig. 6. The signal size gradually decreases with V_0 until an inverse photovoltage is developed in the spectral range between E_{gSiGe} and E_{gSi} (spectrum 3).

The low-energy spectral shape shown in the inset of Fig. 6 appears to be quite complex. In the absence of the strain, the shape exhibits two distinct regions. One of them, above the point marked by the arrow, is formed by $e-h$ pair generation (process 1 in Fig. 7). The tail signal below this point is likely due to electron transport from metal into SiGe above the barrier. Such a tailing is obviously absent in spectrum 2 and this, taken together with the fact that the inverse signal is observed in spectrum 3, implies that the energy bands are bent to the lines shown in Fig. 7(b) in rf strain fields. This forces electrons to move to the SiO_2/SiGe

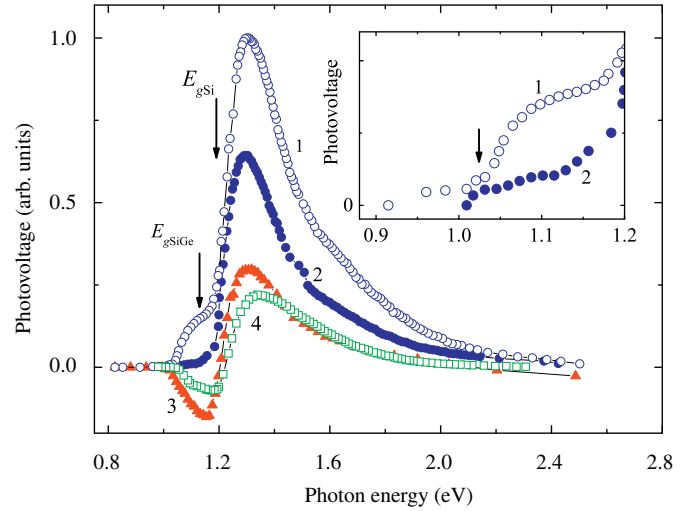


Fig. 6. Room-temperature spectral dependence of the photovoltage in Au/SiGe/Si at applied rf voltage amplitude $V = 0$ (spectrum 1), 23 V (2), 34 V (3). Spectrum 4 illustrates photovoltage spectrum taken in InGa/SiGe/Si at $V = 0$. Spectra 2 and 3 are enlarged by a factor of 10 compared with spectrum 1 whereas spectrum 4 is not in the scale. The inset depicts a square root plot of a low-energy part of spectra 1 and 2.

interface, resulting in a negative voltage and the electron accumulation at the SiGe–oxide interface. Free electrons generated by light migrate to the surface (process 5 in Fig. 7) thus decreasing the photovoltage at $h\nu \geq E_{\text{gSiGe}}$ and finally generating the inverse signal.

In order to support this picture the photovoltage signal was taken with an InGa electrode; see spectrum 4 in Fig. 6. In contrast to Au, which has a workfunction $\approx 0.4 \text{ eV}$ greater than that of Si, the work function of InGa is $\approx 0.5 \text{ eV}$ smaller than that of Si [16,17]. Therefore, the band bending in InGa/SiGe is expected to be opposite to that developed in Au/SiGe and shown in Fig. 7(a). The observed correspondence of spectra 3 and 4 in Fig. 6 therefore supports the suggestion that an inverse band bending indeed occurs in the rf field leading to the inverse photovoltage signal in appropriate spectral range.

In explaining the band bending effect, many potentially relevant factors including accompanying thermal effects, varying defect concentrations in the strain fields, etc., are to be systematically quantified, which warrant careful future study. Here we note that the data are seemingly consistent in several aspects with the dislocation involvement, which has found so far to be the most important parameter in strain-induced modification of electronic parameters in semiconductors [18].

The reason for this is in that peak A rapidly decreases with increasing V_0 , as seen in spectrum 2 of Fig. 4. At higher amplitudes, peak A appears to be completely quenched whereas peak B remains observable (spectrum 3). This observation is consistent with the fact that the dislocation-related DLTS peak may be due to point defects and impurities located in the cloud formed by the dislocation strain field [19]. Therefore, the atomic reconstruction likely occur at the dislocation core in the strain field due to removal of the point defects and impurities away from the core.

In support of this concept, immobile dislocation is known to provide a high stress and stress-gradient environment in which point defect diffusion takes place [20,21]. The relevant theories (e.g., [22,23]) have considered the transition rate as a function of the defect and saddle point energies and position, and the diffusion tensor has been computed from the transition rates. It has been found that the stress effect of dislocations is quite

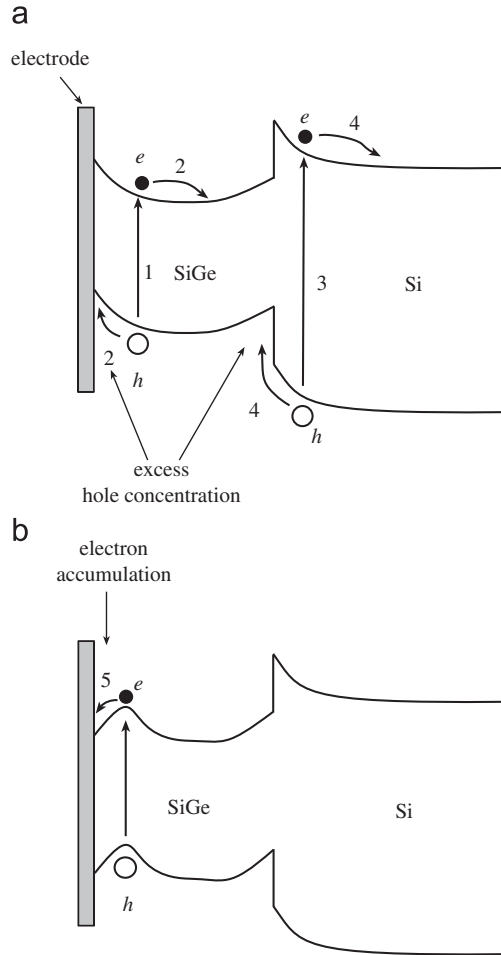


Fig. 7. Energy band diagram for the Au/SiGe/Si structure (a) and (b) suggested rf strain-induced changes in the bands. The generation and electric-field separation of free electrons and holes are shown by arrows 1–5 and explained in the text.

significant. Thus, at a point of local dilatation, the equilibrium vacancy concentration can be reduced by a factor of more than 1000 [23]. On the compression side of the dislocation the effect has been reported to be even stronger.

On the other hand, the response of a crystal containing defects to dynamic loading has also been modelled (e.g., [24] and references therein), illustrating that the defect diffusion can occur via the stress assisted diffusion, and also through the diffusion in the field of inertial forces. Inertia drives atoms from the uncompressed to the compressed regions of the sample and vacancies in the opposite direction, whereas the stress diffusion is associated with the motions opposite to that of the inertial diffusion.

Therefore, these processes should be taken into account, along with the above-modelled strain fields, to accurately describe rf strain-controlled built-in electric fields in our samples, which indicates the need for further computational efforts.

Loosely speaking, if hydrostatic strain is applied, the effect of pressure, p , on the diffusivity, D , is characterized by the activation volume, ΔV , according to [25]

$$-kT \frac{\partial \ln D}{\partial p} = \Delta V, \quad (5)$$

where ΔV is the sum of two components, including (i) the formation volume, which is the volume change in the system upon formation of a defect in its standard state, and (ii) the migration volume, representing the additional volume change

when the defect reaches the saddle point in its migration path. Suppose that $-p = T_{11} + T_{22} + T_{33}$ and the pressure effect is therefore minus the sum of these three uniaxial components.

D usually obeys an Arrhenius law, $D = D_0 \exp(-E_0/kT)$, with the defect migration energy E_0 . If the rf strain field is applied, an extra energy, U , is transmitted to the system of diffused defects, which decreases the defect lifetime with respect to the interstitial diffusion and, hence, lowers the migration energy. Then the diffusivity is

$$D = D_0 \exp(-(E_0 - U)/kT), \quad (6)$$

where the average value of U can be explicitly estimated for the given model [26]

$$U = -\frac{2\Delta V}{3}(T_{11} + T_{22}). \quad (7)$$

Substituting the peak values of $T_{11} + T_{22}$ found to be 1.3×10^7 and 3.3×10^7 Pa for the data of Fig. 3(a) and (b), respectively, and $\Delta V = -0.3\Omega$ with $\Omega = 2 \times 10^{-29} \text{ m}^3$ [27] readily gives a sizeable effect of rf strain on defect diffusivity ($\approx 4.3\%$).

Consistent with the defect migration mechanism, both the photovoltage and DLTS spectra are recovered with a timescale of a few tens of seconds to about 100% of the initial value after the removal of the strain. Therefore, one may imagine that the defects released from the dislocation core affect the surface charge being incorporated into the Si–O– dangling bonds and modify a built-in electric field near SiO₂/SiGe interface. Releasing the strain shifts the dangling bond trapping balance to initial equilibrium value.

5. Summary

The photovoltage signal developed in the Au/SiO₂/SiGe Schottky barrier is found to change its sign in the spectral range from 1 to 1.2 eV in presence of rf strains. This is accompanied by a quenching of DLTS peaks. These effects may be due to accumulation of negative charges at the SiO₂/SiGe interface due to the inverse band bending developed in the strain. More elaborate studies are needed to elucidate the exact picture although the point defect removal from the dislocation core and the defect migration toward the interface are likely involved. This observation opens up new possibilities in manipulating electronic properties of SiGe layers which are relevant to solar cell performance. With the reported technique, a low-cost integrated device implemented on a piezoelectric substrate traversing acoustic waves could be introduced, in which built-in fields at the interface are controlled by an rf voltage applied to the substrate.

Acknowledgements

Financial support of the Ministry of Education and Science of Ukraine is gratefully acknowledged.

References

- [1] H. Presting, Near and mid infrared silicon/germanium based photodetection, *Thin Solid Films* 321 (1998) 168–195.
- [2] S. Tong, J.L. Liu, J. Wang, K.L. Wang, Normal-incidence Ge quantum-dot photodetectors at 1.5 μm based on Si substrate, *Appl. Phys. Lett.* 80 (2002) 1189–1191.
- [3] C. Miesner, K. Brunner, G. Abstreiter, Lateral photodetectors with Ge quantum dots in Si, *Infrared Phys. Technol.* 42 (2001) 461–465.
- [4] H. Presting, J. Konle, H. Kibbel, Self-assembled Ge-dots for Si solar cells, *Int. J. Mod. Phys. B* 16 (2003) 4347–4351.
- [5] S. Ostapenko, N.E. Korsunskaya, M.K. Sheinkman, Ultrasound stimulated defect reactions in semiconductors, *Solid State Phenom.* 85–86 (2002) 317–336.

- [6] S. Ostapenko, L. Jastrzebski, J. Lagowski, R.K. Smeltzer, Enhanced hydrogenation in polycrystalline silicon thin films using low-temperature ultrasound treatment, *Appl. Phys. Lett.* 68 (1996) 2873–2875.
- [7] S.S. Ostapenko, R.E. Bell, Ultrasound stimulated dissociation of Fe–B pairs in silicon, *J. Appl. Phys.* 77 (1995) 5458–5460.
- [8] V.D. Krevchik, R.A. Muminov, A.Ya. Yafasov, Influence of ultrasound on ionic diffusion process in semiconductors, *Phys. Status Solidi (a)* 63 (1981) K159–K162.
- [9] I.V. Ostrovskii, O.A. Korotchenkov, Influence of nuclear radiation and ultrasound treatment on the photoconductivity of silicon, *Sov. Phys. Tech. Phys.* 56 (1986) 2283–2284.
- [10] Ya.M. Olikh, M.D. Tymochko, A.P. Dolgolenko, Acoustic-wave-stimulated transformations of radiation defects in γ -irradiated *n*-type silicon crystals, *Tech. Phys. Lett.* 32 (2006) 66–73.
- [11] N.A. Guseynov, Ya.M. Olikh, Sh.G. Askerov, Ultrasonic treatment restores the photoelectric parameters of silicon solar cells degraded under the action of ^{60}Co gamma radiation, *Tech. Phys. Lett.* 33 (2007) 38–44.
- [12] T. Makkonen, A. Holappa, J. Ella, M.M. Salomaa, Finite element simulations of thin-film composite BAW resonators, *IEEE Trans. Ultrason. Ferroelect. Freq. Control* 48 (2001) 1241–1258.
- [13] B.A. Auld, *Acoustic Fields and Waves in Solids*, vol. 1, Wiley, New York, 1973.
- [14] C.G. Ahn, H.S. Kang, Y.K. Kwon, S.M. Lee, B.R. Ryum, B.K. Kang, Oxidation-induced traps near SiO_2/SiGe interface, *J. Appl. Phys.* 86 (1999) 1542–1547.
- [15] G.L. Benton, L.C. Kimerling, Capacitance transient spectroscopy of trace contamination in silicon, *J. Electrochem. Soc.* 129 (1982) 2098–2102.
- [16] A.O. Evwaraye, E. Sun, Electron-irradiation-induced divacancy in lightly doped silicon, *J. Appl. Phys.* 47 (1976) 3776–3780.
- [17] B.G. Svensson, M. Willander, Generation of divacancies in silicon irradiated by 2-MeV electrons: depth and dose dependence, *J. Appl. Phys.* 62 (1987) 2758–2762.
- [18] I.V. Ostrovskii, O.A. Korotchenkov, T. Goto, H.G. Grimmeiss, Sonoluminescence and acoustically driven optical phenomena in solids and solid–gas interfaces, *Phys. Rep.* 311 (1999) 1–46.
- [19] M. Kittler, W. Seifert, K. Knobloch, Influence of contamination on the electrical activity of crystal defects in silicon, *Microelectr. Eng.* 66 (2003) 281–288.
- [20] J.S. Koehler, Diffusion of lattice defects in a stress field, *Phys. Rev.* 181 (1969) 1015–1019.
- [21] C.P. Flynn, *Point Defects and Diffusion*, Clarendon, Oxford, 1972.
- [22] P.H. Dederichs, K. Schroeder, Anisotropic diffusion in stress fields, *Phys. Rev. B* 17 (1978) 2524–2536.
- [23] D.L. Olmsted, R. Phillips, W.A. Curtin, Modelling diffusion in crystals under high internal stress gradients, *Modelling Simul. Mater. Sci. Eng.* 12 (2004) 781–797.
- [24] Yu. Skryl, M.M. Kuklja, Diffusion of point defects in shocked molecular crystals, *Phys. Rev. B* 71 (2005) 094109 (8 pages).
- [25] R.N. Jeffery, D. Lazarus, Calculating activation volumes and activation energies from diffusion measurement, *J. Appl. Phys.* 41 (1970) 3186–3187.
- [26] M.J. Aziz, Y. Zhao, H.-J. Gossmann, S. Mitha, S.P. Smith, D. Schiferl, Pressure and stress effects on the diffusion of B and Sb in Si and Si–Ge alloys, *Phys. Rev. B* 73 (2006) 054101 (20 pages).
- [27] A. Antonelli, J. Bernholc, Pressure effects on self-diffusion in silicon, *Phys. Rev. B* 40 (1989) 10643–10646.